

# Imaging Electric and Magnetic Modes and Their Hybridization in Single and Dimer AlGaAs Nanoantennas

Cillian P. T. McPolin,<sup>\*</sup> Giuseppe Marino, Alexey V. Krasavin, Valerio Gili, Luca Carletti, Costantino De Angelis, Giuseppe Leo, and Anatoly V. Zayats

All-dielectric nanoantennas enable the manipulation and confinement of light on the nanoscale through a variety of resonant excitations. Understanding and controlling the interactions among resonances at a level of individual nanoantennas is required for the development of appropriate design rules for their applications, especially with regard to nonlinear optics, where the nonlinear interaction depends on the resonant behavior in a superlinear manner. Here, cathodoluminescence imaging spectroscopy is used to experimentally investigate the electric and magnetic modes supported by single AlGaAs nanoantennas and their hybridization in a dimer configuration. An interplay is shown between the resonant modes of the nanostructures and interband emission of the semiconductor material, which contrasts with Si nanoantennas, where the bandgap effects are not significant. The measurements are in very good agreement with numerical simulations, which also provided further insight into the nature of the modes. The resonant modes of semiconductor nanoantennas are important for engineering linear and nonlinear metasurfaces, as well as for sensing applications and fluorescence control in nanophotonic environments.

## 1. Introduction

The ability to manipulate, confine and redirect light on the nanoscale is essential in the development of photonic devices, metamaterials and metasurfaces, as well as for integrated optical applications, including solar cells and sensors. To this end, optical nanoantennas enable the collection and confinement of light to volumes smaller than the diffraction

limit, and may also serve to enhance and direct the emission from local sources. In both regards, the antennas act as a crucial bridge between the electromagnetic radiation in the far- and near-field regions, and have recently attracted considerable attention.<sup>[1]</sup> Metal-based nanoantennas, composed of materials such as silver and gold, harness the properties of plasmonic excitations to control light on the nanoscale, opening up many opportunities within areas such as telecommunications, sensing, and photovoltaics.<sup>[2–4]</sup> The plasmonic response of such nanoantennas stems from the collective oscillation of electrons,<sup>[5]</sup> which enables significant enhancement of the electric near-field, whereas the magnetic near-field is not considerably affected. However, the inherent ohmic loss associated with plasmonic excitations gives rise to Joule heating and, as a result, their use in temperature-sensitive applications, such as surface enhanced

Raman spectroscopy, might be hindered.<sup>[6,7]</sup>

By contrast, all-dielectric and semiconductor nanoantennas composed of high-index materials in a low-index background may support both electric and magnetic Mie-type resonances, therefore facilitating significant field confinement whilst maintaining low losses across the visible and near-infrared spectral regions.<sup>[8–13]</sup> These dielectric or semiconductor nanoantennas confine fields within the volume of the structure, which results in lower field confinement compared to their metallic counterparts, but also allows for a greater effective interaction volume between the incident field and the bulk material in, for example, nonlinear processes.<sup>[6]</sup> All-dielectric nanophotonic technology can be readily employed in loss- and temperature-sensitive applications.<sup>[14]</sup> Moreover, interplay between electric and magnetic resonances in these nanoantennas provides a means of engineering the directionality of scattering and second-harmonic generation.<sup>[15–18]</sup> Consequently, arrays of dielectric nanoantennas represent a promising route toward low-loss metamaterials and metasurfaces,<sup>[16,19,20]</sup> in addition to nanoscale photodiodes.<sup>[21]</sup> Moreover, destructive interference between two different dipole moments in nanoscale antennas may lead to nonradiative anapole modes.<sup>[22,23]</sup> Importantly, dielectric nanoantennas are suitable for engineering nonlinear optical effects if they are composed of materials with a high nonlinear susceptibility, such as GaAs<sup>[24]</sup> and AlGaAs.<sup>[6]</sup>

Dr. C. P. T. McPolin, Dr. G. Marino, Dr. A. V. Krasavin, Prof. A. V. Zayats  
Department of Physics  
King's College London  
Strand, London WC2R 2LS, UK  
E-mail: cillian.mcpolin@kcl.ac.uk

Dr. G. Marino, Dr. V. Gili, Dr. G. Leo  
Matériaux et Phénomènes Quantiques  
Université Paris Diderot-CNRS  
10 rue Alice Domon et Léonie Duquet, 75013 Paris, France

Dr. L. Carletti, Prof. C. De Angelis  
Department of Information Engineering  
University of Brescia  
Via Branze 38, 25123 Brescia, Italy

 The ORCID identification number(s) for the author(s) of this article can be found under <https://doi.org/10.1002/adom.201800664>.

DOI: 10.1002/adom.201800664

The large effective interaction volumes, and low inherent losses, permit dielectric nanoantennas to sustain large optical powers, hence making them advantageous for nonlinear applications. In addition, the nonlinear polarizabilities may be enhanced by the multipolar nature of the electric and magnetic modes, with their interplay also establishing a means for controlling the directionality of nonlinear emission.<sup>[6,25–28]</sup> High nonlinear efficiencies provide a wide range of possible applications,<sup>[29]</sup> including nonlinear microscopy, holography, and the achievement of efficient quantum-entangled light sources through spontaneous parametric down-conversion.<sup>[9]</sup>

With respect to the nanoantenna geometry, a nanopillar (cylindrical) design is particularly beneficial as it offers two degrees of freedom, namely, diameter and height, which permits tuning of the electric and magnetic modes. Additionally, dimers, which are composed of two nanopillars with a sub-wavelength gap, may also support magnetic hotspots,<sup>[30]</sup> that, along with electric hotspots, influence the local density of states.<sup>[31]</sup> All-dielectric dimer structures have also been used to enhance fluorescence,<sup>[7,32]</sup> and enable greater control over the direction of emission compared to single particles.<sup>[33,34]</sup> Coupling between adjacent nanopillars has been shown to give rise to hybridization of the electric and magnetic modes, which has previously been observed using silicon nanoparticles.<sup>[35]</sup> Crucially, in order to effectively harness the properties of such dielectric nanoantennas, the nature of resonances supported by single and coupled nanoantennas must be fully explored and understood.

In this paper, we experimentally study the electric and magnetic resonances supported by individual AlGaAs nanopillars in the visible and infrared spectral ranges and the hybridized modes present in individual dimers, using cathodoluminescence (CL) imaging spectroscopy. By scanning a focused electron beam across the nanoantennas, we reveal the resonances that are inaccessible under the plane wave illumination and investigate the interplay between the resonances and bandgap emission in the nanoantenna material. The CL emission was measured from single pillars of different diameters so that the dependence of the supported modes on the aspect ratio and size of the nanopillars can be revealed. Additionally, the spectral and spatial characteristics of the dimer resonances were investigated, showing hybridization of the electric and magnetic modes. The experimental results exhibited very good agreement with numerical calculations, which allowed the electric or magnetic character of the resonances to be identified.

## 2. Results and Discussion

The geometry of the nanoantennas is outlined in **Figure 1a**, for both single and dimer configurations. The height,  $h$ , of the fabricated nanopillars is fixed at 400 nm, while the diameter,  $d$ , and dimer separation,  $s$ , are varied. These nanostructures support

both magnetic and electric optical resonances as a consequence of their size, high index and low absorption losses. Excitation of magnetic modes occurs due to the coupling to displacement current loops, while electric modes arise as a result of collective polarization,<sup>[36,37]</sup> leading to characteristic field distributions of magnetic and electric multipoles. Due to the symmetry of the nanopillars, the horizontal magnetic and electric dipole modes are degenerate in all in-plane directions.

In order to characterize the response of the nanoantennas, CL imaging spectroscopy was employed (see the Experimental Section for details), in addition to numerical simulations. **Figure 1b** illustrates a scanning electron microscope image of a nanopillar, where  $d = 400$  nm. The corresponding CL intensity map at a wavelength of 730 nm is due to band-edge emission of the semiconductor (**Figure 1c**). In this case, the strongest CL emission occurs when the e-beam is positioned at the center of the nanopillar, due to symmetry. Moreover, the CL spectra of individual nanopillars of different diameters, excited in the center, all exhibit this band-edge peak, which is evidently insensitive to the size of the pillars (**Figure 2a,b**). The experimental measurements and modeling spectra displayed very good correspondence in a frequency range below the bandgap (at the wavelengths longer than  $\approx 730$  nm), whereas above the bandgap the CL signal is significantly suppressed. This behavior contrasts with, for example, Si nanoantennas, where the role of interband emission is not significant and, therefore, experimentally measured resonances are clearly visible in the CL spectra above the bandgap.<sup>[35,38]</sup> Examination of the simulated eigenmode electric field profiles for these structures allowed for identification of electric (**Figure 2d,f,h,j**) and magnetic (**Figure 2c,e,g,i**) modes at the resonance peaks. Here, we note that theoretical study and identification of the resonances in single and dimer nanocylinders of finite length can only be done by semianalytical<sup>[39]</sup> or numerical<sup>[31]</sup> means, as analytical closed form solutions in these cases are unobtainable.<sup>[40]</sup>

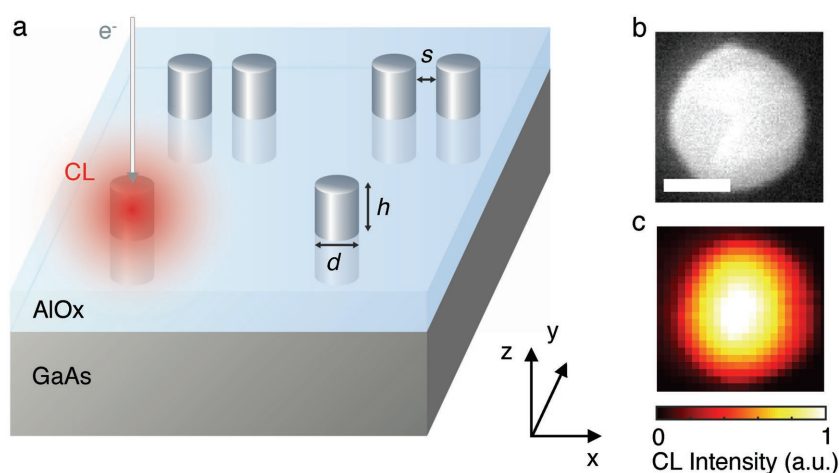


**Figure 1.** Structure of the AlGaAs nanoantennas and their characterization using cathodoluminescence. a) Single pillars with height  $h$ , diameter  $d$ , and dimers, with a separation  $s$ . b) Scanning electron microscope image of a nanopillar with  $d = 400$  nm, and c) corresponding CL intensity map, at a wavelength of 730 nm with a pixel size of 20 nm and bandwidth of 30 nm, where the CL signal is predominantly due to band-edge emission of the semiconductor. The scale bar in (b) is 200 nm.

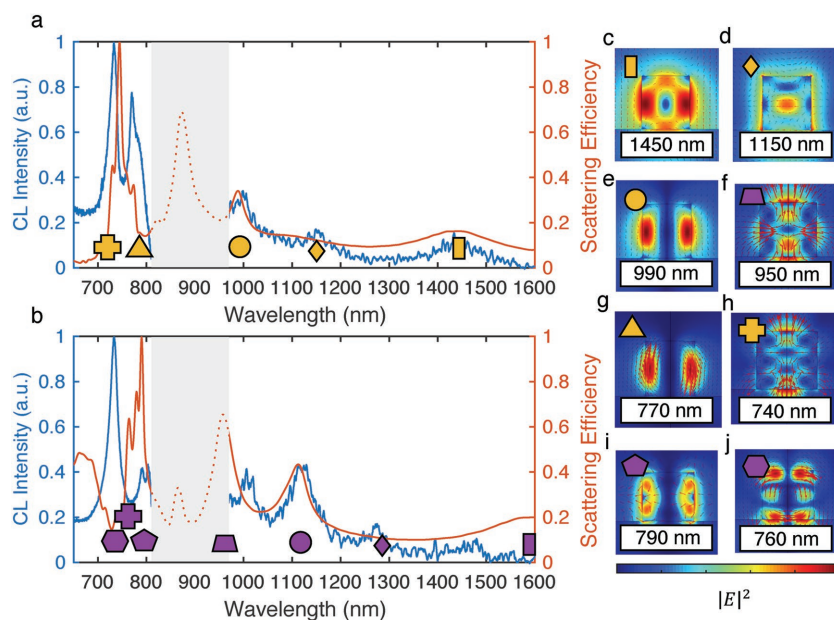


**Figure 2.** CL spectra for single AlGaAs pillars with a)  $d = 360$  nm and b)  $d = 420$  nm, due to e-beam excitation at the center of the nanopillars: (blue lines) experimental CL measurements and (red lines) simulations using dipole excitation. Grey shading indicates the spectral range wherein CL emission from the nanopillars is obscured by CL emission from the substrate. c–j) Eigenmode simulations showing the electric field distributions for the modes supported by the nanopillars in the visible and near-infrared region: (c,e,g,i) magnetic modes and (d,f,h,j) electric modes. Field distributions are cross-sections of the electric field intensity taken along the  $x$ - $z$  plane through the center of the nanopillars. The corresponding spectral positions of the modes are indicated in (a) and (b) with colored markers, where each shape corresponds to a specific mode.

For all the nanopillar diameters studied, high-order resonances manifest in the visible region, whilst predominantly dipolar and quadrupolar modes are supported in the infrared. Considering the 360 nm diameter nanopillar, Figure 2a illustrates a resonance at 770 nm that is in good agreement with the corresponding simulation, which is shown to be magnetic in its origin (Figure 2g). However, the simulated peak at 740 nm (Figure 2h), is not displayed in the experiment, as it is likely hidden by the large band-edge luminescence at 730 nm. In the infrared region, there are three peaks at 1450, 1150, and 990 nm which are closely mirrored by the simulations. These resonances are due to the excitation of magnetic dipolar, electric dipolar, and magnetic quadrupolar modes, respectively, as identified by the mode field distributions (Figures 2c–e).

In the case of the 420 nm diameter nanopillar (Figure 2b), the experimental resonances at around 790 and 800 nm are in good agreement with the simulations (780 and 790 nm, respectively), with a slight red-shift possibly due to a difference in size or a deviation from a pillar shape (e.g., tapering). A peak corresponding to the simulated resonance at 760 nm is not evident in the CL measurement, as it may be masked by the resonance at 790 nm. In this case, there are four infrared peaks at 1005, 1120, 1270, and  $\approx 1500$  nm, which exhibit good agreement with the simulations, with the exception of the resonance at 1270 nm, which is not perceptible in the simulated spectrum as it is likely hidden by the broad magnetic dipole resonance

at  $\approx 1600$  nm. Additionally, the sensitivity of the CL system drops sharply toward 1600 nm, and therefore the experimental peak at 1500 nm may extend further into the infrared, in line with the simulations.

Comparing the two diameters, it is obvious that an increase in diameter yields both a general red-shift in the resonances, and change of their spectral separation, leading to an overlap of the electric and magnetic modes. In particular, the three infrared resonances evident in Figure 2a are shown to red-shift in Figure 2b. This enables the tuning of the spectral response of the nano-antennas via altering their diameters and is hence particularly advantageous for many applications requiring a specific wavelength of operation.

In the case of dimer structures, the coupling between adjacent nanopillars also gives rise to hybridization, yielding symmetric and antisymmetric bonding modes that provide a greater opportunity for engineering their emission and confinement properties. Normal incidence plane wave illumination is only able to excite symmetric modes, where the dipole moments are parallel, whereas excitation using a quasi-point-like e-beam allows for the investigation of both symmetric and antisymmetric modes. These antisymmetric modes concentrate energy and contribute to the local density of states. Figure 3a outlines the CL spectrum acquired when a dimer (individual pillar diameter of 330 nm and separation of 110 nm) is illuminated at various positions with an e-beam. Peaks at 1100, 1200, and 1350 nm are apparent, which are broader compared to the single pillar spectra (Figure 2a,b). This is borne out by the corresponding simulation (Figure 3f), which also displays a variation in the peaks intensity and wavelength as the excitation position is altered. In particular, the magnitude of the peak at 1200 nm is shown to vary significantly (Figure 3a,f). Moreover, spectra calculated via the eigenmode simulations (Figure 3g), illustrate multiple resonances that overlap to produce the broad peaks observed in the experiment. By contrast, plane wave excitation of the dimer at the normal incidence (Figure S1, Supporting Information) exhibits only two resonances for each incident polarization, corresponding to the excitation of the symmetric modes.

Figure 3b–e illustrates maps of the CL intensity at the wavelengths 1000, 1100, 1200, and 1350 nm, respectively. These maps highlight the spectral variation in the CL distribution that arises due to the interplay of the contributing modes. For instance, the CL map shown in Figure 3e is predominantly the result of the three magnetic modes residing in the wavelength range 1330–1410 nm. Additionally, when considering the linewidths exhibited in Figure 3g, the two antisymmetric mode peaks in the aforementioned range are narrower than the symmetric ones, suggesting lower

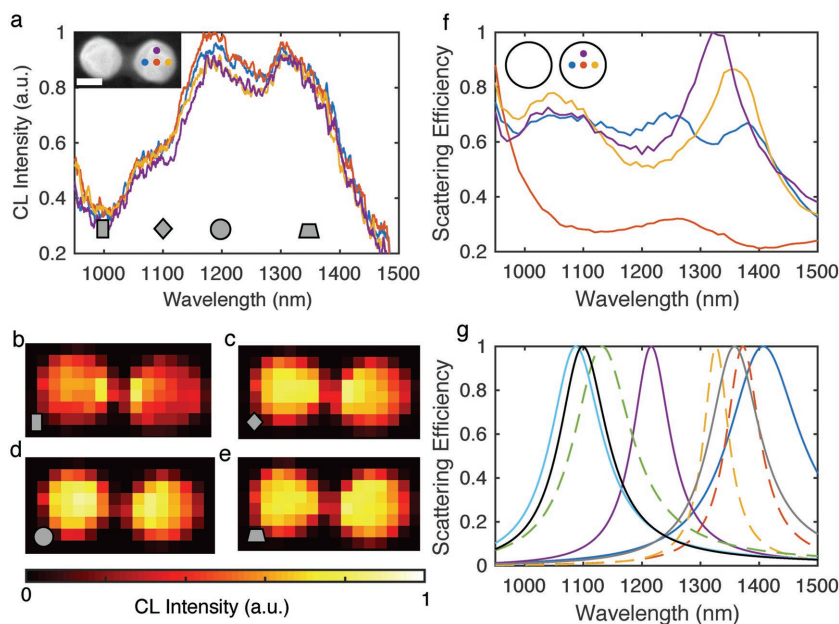


**Figure 3.** CL emission from an AlGaAs dimer with  $s = 110$  nm and an individual pillar  $d = 330$  nm. a) Experimental CL spectra with the corresponding excitation positions shown in the inset. The scale bar is 200 nm. b–e) CL intensity maps for the wavelengths 1000, 1100, 1200, and 1350 nm, respectively, with a pixel size of 60 nm. The spectral positions of the maps are indicated in (a). The bandwidth for each map is 30 nm. f) Simulated spectra for the dimer under dipole excitation, with the corresponding excitation positions shown in the inset. g) Spectra calculated via the eigenmode simulations, showing the peak positions and spectral widths of the individual modes. Solid and dashed colored lines correspond to symmetric and antisymmetric modes in the dimer, respectively. The electric and magnetic dipole modes present in an isolated pillar with  $d = 330$  nm are shown by black and grey solid lines, respectively.

radiative losses, and, therefore, a greater contribution to the CL map may originate from the symmetric mode. Significantly, Figure 3b displays CL hotspots at the nanopillar edges closest to

the visibility of individual mode distributions. Nonetheless, the CL profiles display a degree of correspondence with the individual simulated field profiles (cf. Figure 3b–e and

one another, with the asymmetry confirming the presence of mode hybridization. This asymmetric CL profile likely corresponds to an antisymmetric electric mode, as illustrated in Figure 4a.

A detailed overview of the specific dimer modes is provided in Figure 4, which displays the electric field distributions of the eigenmodes. The three antisymmetric electric and magnetic modes cannot be excited under normal incidence plane wave illumination (Figure 4a–c). There is strong spectral overlap between the multiple symmetric and antisymmetric modes, giving rise to the broad peaks (Figure 3a,f). It is evident from Figure 3g that the symmetric and antisymmetric electric dipole modes both occur in the spectral vicinity of the isolated electric dipole mode, which manifests at 1100 nm, as can be expected. All four possible alignments of the magnetic dipole modes reside in the region 1220–1410 nm, around the isolated magnetic dipole mode at 1360 nm. This splitting of the original single pillar modes is a hallmark of hybridization, confirming the coupling between the two nanopillars. Additionally, the coupling strength will manifestly depend on their separation, which represents another degree of freedom for tuning their optical properties. It is also worth noting that the CL profiles are due to multiple modes being concurrently excited, which hinders

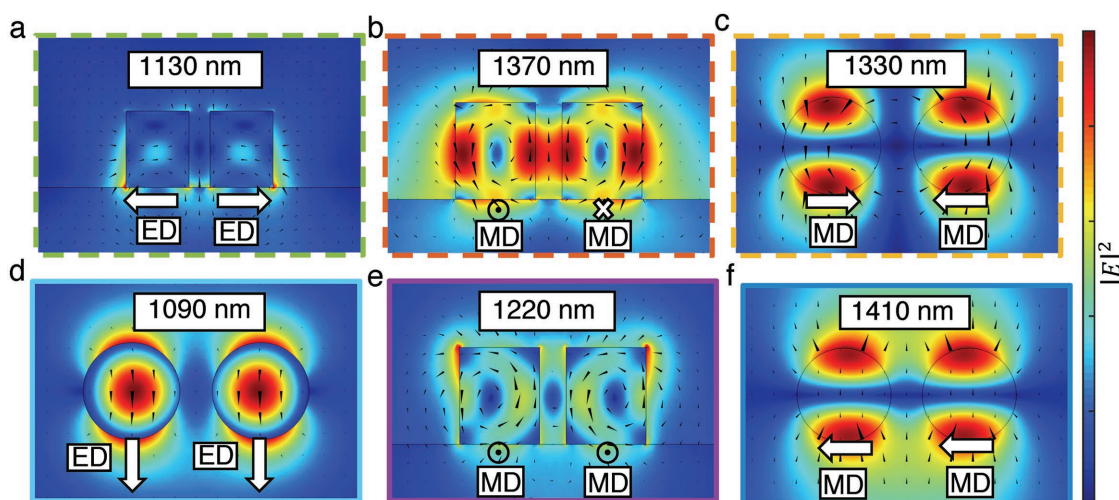


**Figure 4.** Simulated eigenmode electric field profiles for the dimer nanopillar considered in Figure 3. a–c) Antisymmetric modes and d–f) symmetric modes. The field distributions are cross-sections of the electric field intensity taken through the center of the nanopillars along a,b,e) the  $x$ - $z$  and c,d,f) the  $x$ - $y$  planes. The directions of the electric and the magnetic dipoles are shown, together with the wavelengths. Color frames correspond to the peaks in Figure 3g.

Figure 4), which further indicates the field distribution of the modes.

It is apparent that, depending on the excitation position of the dimer, different modes are preferentially excited (cf. Figure 4 and Figure 3a,f). In other words, efficient driving of a specific mode occurs when the highly localized electric field generated by the e-beam overlaps the electric field of the eigenmode. Moreover, the e-beam induced coherent radiation, which arises due to electrons passing across the sample interface (the predominant radiation source below the bandgap), was represented as a vertical dipole in the very first approximation.<sup>[38]</sup> As the dipole is orientated vertically along the direction of the e-beam current, it will strongly excite modes that possess a vertical electric field component at its position. This ability to preferentially excite different modes depending on the illumination position also paves the way for greater control of the directionality of the radiation pattern and the Purcell effect for individual quantum emitters strategically positioned with respect to nanopillars.

### 3. Conclusion

We have experimentally demonstrated electric and magnetic resonances in both single and dimer AlGaAs nanoantennas. CL imaging spectroscopy provided direct confirmation of the modes in both the visible and infrared spectral ranges. The modes were subsequently analyzed via numerical simulations, allowing their electric or magnetic character to be ascertained. The dimers support multiple hybridized modes that spectrally overlap, giving rise to the broad peaks observed in the CL spectra. The spectra vary significantly as the electron beam moves across the dimer, illustrating the preferential excitation of different modes with the variation of the excitation position. The results verify that the modes of individual and coupled nanoantennas can be effectively characterized, leading to a fuller understanding of their optical properties. This is a necessary step in the development of nanoantennas with specific emission and confinement characteristics, for enabling a greater range of potential applications.

### 4. Experimental Section

**Sample Fabrication:** The design and fabrication procedure of the nanopillars are summarized in Figure S2 of the Supporting Information. AlGaAs was chosen as the constituent material for the nanoantennas, due to its compatibility with nanophotonic technology, permitting integration with optical sources and detectors. Moreover, recent advances in nonconventional CMOS-compatible fabrication processes have established AlGaAs as a viable alternative platform to Si, especially with regard to applications involving quadratic nonlinearities.<sup>[41]</sup> A 400 nm layer of  $\text{Al}_{0.18}\text{Ga}_{0.82}\text{As}$ , on top of a 1  $\mu\text{m}$  thick  $\text{Al}_{0.98}\text{Ga}_{0.02}$  layer sandwiched between two transition regions with linearly varying aluminum molar fraction, was grown by molecular-beam-epitaxy on a [100] nonintentionally doped GaAs wafer. An array of nanopillars was realized by patterning circles with diameters between 300 and 450 nm, and equally spaced by 3  $\mu\text{m}$ , with a scanning electron microscope lithography system. The samples were subsequently dry etched with nonselective ICP-RIE with  $\text{SiCl}_4\text{:Ar}$  chemical treatment. The etching depth of 400 nm, controlled by laser interferometer, defined the

nanopillars and revealed the AlAs layer. The etched sample was then oxidized at 390 °C for 30 min in an oven equipped with in situ optical monitoring, under a precisely controlled water vapor flow with  $\text{N}_2\text{:H}_2$  carrier gas. After oxidation, each  $\text{Al}_{0.18}\text{Ga}_{0.82}\text{As}$  nanopillar remained on a uniform  $\text{AlO}_x$  substrate, whose low refractive index enables sub-wavelength optical confinement in the nanocavity by total internal reflection.

**Simulations:** Full-vectorial electromagnetic simulations implemented with the finite element method in the COMSOL software were used to investigate the modal structure of single and dimer nanopillars. In the simulation domain, the  $\text{Al}_{0.18}\text{Ga}_{0.82}\text{As}$  nanopillars were standing in air ( $n = 1$ ) on a uniform semi-infinite  $\text{AlO}_x$  substrate ( $n = 1.6$ ). The dispersion of the complex permittivity of  $\text{Al}_{0.18}\text{Ga}_{0.82}\text{As}$  was modeled from the experimental data.<sup>[42]</sup> Open boundary conditions were simulated using perfectly matched layers. The optical excitation was implemented with a single point dipole source of unitary amplitude. The scattering efficiencies were subsequently calculated as the ratio of the outgoing flux of the Poynting vector generated by the point dipole source with and without the nanostructures. Eigenfrequencies and spatial electric field profiles of the nanostructure modes were calculated with an eigenmode analysis implemented in COMSOL.

**Experiment:** CL measurements were carried out using a commercial system (SPARC, Delmic). In order to characterize the CL emission, a focused 30 keV electron beam was scanned across the sample surface, acting as a broadband nanoscale light source for the local excitation of the antennas, thereby providing sub-wavelength resolution.<sup>[43,44]</sup> Moreover, due to the high localization, the electron beam can excite modes that are momentum- and symmetry-forbidden for a plane wave.<sup>[35,43]</sup> Upon e-beam illumination, the excited modes subsequently radiate into the far-field, with the signal collected by a parabolic mirror and directed into a spectrometer (Figure S3, Supporting Information). The e-beam was scanned across the sample, yielding 2D CL intensity maps. The CL signal was averaged over the pixels corresponding to the region of interest, to produce CL spectra (Figures 2a,b and 3a). CL originating from the GaAs substrate exhibits a peak at a wavelength of 870 nm that obscures emission from the nanopillars, and thus no measurements were possible within its spectral vicinity. This background CL, measured when the substrate was directly illuminated, was subtracted from each measurement. This results in an artificial drop in signal near 870 nm, due to the inherently larger background signal acquired when the substrate is directly excited, compared to indirect excitation of the substrate when the nanopillars are illuminated. CL spectra in the visible and infrared regions (Figure 2a,b, left and right of the gray region) were acquired sequentially, as efficient collection of CL in both regions required a change in optics and camera. Sensitivity in the infrared region is inherently lower than in the visible region, which necessitated longer exposure times. The infrared CL spectra were also filtered in MATLAB. An estimation of the magnitude of CL signal in the infrared region relative to the visible was carried out via comparison with the corresponding simulations (Figure 2a,b). It is important to note that CL imaging provides information exclusively on radiative modes (i.e., modes that couple to far-field radiation), whereas, for example, electron energy loss spectroscopy<sup>[45,46]</sup> probes both the radiative and nonradiative density of states.<sup>[47]</sup>

### Supporting Information

Supporting Information is available from the Wiley Online Library or from the author.

### Acknowledgements

This work was supported in part by EPSRC (UK) and the ERC iPLASMM project (321268). The authors gratefully acknowledge partial financial support from the Erasmus Mundus NANOPHI program. A.Z.

acknowledges support from the Royal Society and the Wolfson Foundation. G.L. acknowledges financial support from SATT IdF-Innov and the SEAM Labex (PANAMA structuring project). The data access statement: all data supporting this research are provided in full in the results section and supporting information.

## Conflict of Interest

The authors declare no conflict of interest.

## Keywords

cathodoluminescence, dielectric nanoantennas, nanophotonics

Received: May 21, 2018

Revised: June 27, 2018

Published online:

- [1] L. Novotny, N. van Hulst, *Nat. Photonics* **2011**, 5, 83.
- [2] V. Giannini, A. I. Fernandez-Dominguez, S. C. Heck, S. A. Maier, *Chem. Rev.* **2011**, 111, 3888.
- [3] S. B. Hasan, F. Lederer, C. Rockstuhl, *Mater. Today* **2014**, 17, 478.
- [4] T. Coenen, F. B. Arango, A. F. Koenderink, A. Polman, *Nat. Commun.* **2014**, 5, 3250.
- [5] A. V. Zayats, I. I. Smolyaninov, A. A. Maradudin, *Phys. Rep.* **2005**, 408, 131.
- [6] L. Carletti, A. Locatelli, O. Stepanenko, G. Leo, C. De Angelis, *Opt. Express* **2015**, 23, 26544.
- [7] M. Caldarola, P. Albella, E. Cortes, M. Rahmani, T. Roschuk, G. Grinblat, R. F. Oulton, A. V. Bragas, S. A. Maier, *Nat. Commun.* **2015**, 6, 7915.
- [8] A. E. Krasnok, A. E. Miroshnichenko, P. A. Belov, Y. S. Kivshar, *Opt. Express* **2012**, 20, 20599.
- [9] A. I. Kuznetsov, A. E. Miroshnichenko, M. L. Brongersma, Y. S. Kivshar, B. Luk'yanchuk, *Science* **2016**, 354, 846.
- [10] A. I. Kuznetsov, A. E. Miroshnichenko, Y. H. Fu, J. Zhang, B. Luk'yanchuk, *Sci. Rep.* **2012**, 2, 492.
- [11] M. K. Schmidt, R. Esteban, J. J. Saenz, I. Suarez-Lacalle, S. Mackowski, J. Aizpurua, *Opt. Express* **2012**, 20, 13636.
- [12] D. S. Filonov, A. E. Krasnok, A. P. Slobozhanyuk, P. V. Kapitanova, E. A. Nenasheva, Y. S. Kivshar, P. A. Belov, *Appl. Phys. Lett.* **2012**, 100, 201113.
- [13] A. B. Evlyukhin, S. M. Novikov, U. Zywietz, R. L. Eriksen, C. Reinhardt, S. I. Bozhevolnyi, B. N. Chichkov, *Nano Lett.* **2012**, 12, 3749.
- [14] L. Carletti, A. Locatelli, D. Neshev, C. De Angelis, *ACS Photonics* **2016**, 3, 1500.
- [15] Y. H. Fu, A. I. Kuznetsov, A. E. Miroshnichenko, Y. F. Yu, B. Luk'yanchuk, *Nat. Commun.* **2013**, 4, 1527.
- [16] J. Li, N. Verellen, D. Vercrussse, T. Bearda, L. Lagae, P. Van Dorpe, *Nano Lett.* **2016**, 16, 4396.
- [17] J. M. Geffrin, B. Garcia-Camara, R. Gomez-Medina, P. Albella, L. S. Froufe-Perez, C. Eyraud, A. Litman, R. Vaillon, F. Gonzalez, M. Nieto-Vesperinas, J. J. Saenz, F. Moreno, *Nat. Commun.* **2012**, 3, 1171.
- [18] S. V. Li, D. G. Baranov, A. E. Krasnok, P. A. Belov, *Appl. Phys. Lett.* **2015**, 107, 171101.
- [19] S. Jahani, Z. Jacob, *Nat. Nanotechnol.* **2016**, 11, 23.
- [20] D. Lin, P. Fan, E. Hasman, M. L. Brongersma, *Science* **2014**, 345, 298.
- [21] M. Garin, R. Fenollosa, R. Alcubilla, L. Shi, L. F. Marsal, F. Meseguer, *Nat. Commun.* **2014**, 5, 3440.
- [22] A. E. Miroshnichenko, A. B. Evlyukhin, Y. F. Yu, R. M. Bakker, A. Chipouline, A. I. Kuznetsov, B. Luk'yanchuk, B. N. Chichkov, Y. S. Kivshar, *Nat. Commun.* **2015**, 6, 8069.
- [23] G. Grinblat, Y. Li, M. P. Nielsen, R. F. Oulton, S. A. Maier, *ACS Nano* **2017**, 11, 953.
- [24] S. Liu, M. B. Sinclair, S. Saravi, G. A. Keeler, Y. Yang, J. Reno, G. M. Peake, F. Setzpfandt, I. Staude, T. Pertsch, I. Brener, *Nano Lett.* **2016**, 16, 5426.
- [25] L. Carletti, D. Rocco, A. Locatelli, C. De Angelis, V. F. Gili, M. Ravaro, I. Favero, G. Leo, M. Finazzi, L. Ghirardini, M. Celebrano, G. Marino, A. V. Zayats, *Nanotechnology* **2017**, 28, 114005.
- [26] R. Camacho-Morales, M. Rahmani, S. Kruk, L. Wang, L. Xu, D. A. Smirnova, A. S. Solntsev, A. Miroshnichenko, H. H. Tan, F. Karouta, S. Naureen, K. Vora, L. Carletti, C. De Angelis, C. Jagadish, Y. S. Kivshar, D. N. Neshev, *Nano Lett.* **2016**, 16, 7191.
- [27] V. F. Gili, L. Carletti, A. Locatelli, D. Rocco, M. Finazzi, L. Ghirardini, I. Favero, C. Gomez, A. Lemaitre, M. Celebrano, C. De Angelis, G. Leo, *Opt. Express* **2016**, 24, 15965.
- [28] M. R. Shcherbakov, D. N. Neshev, B. Hopkins, A. S. Shorokhov, I. Staude, E. V. Melik-Gaykazyan, M. Decker, A. A. Ezhov, A. E. Miroshnichenko, I. Brener, A. A. Fedyanin, Y. S. Kivshar, *Nano Lett.* **2014**, 14, 6488.
- [29] M. R. Shcherbakov, P. P. Vabishchevich, A. S. Shorokhov, K. E. Chong, D. Y. Choi, I. Staude, A. E. Miroshnichenko, D. N. Neshev, A. A. Fedyanin, Y. S. Kivshar, *Nano Lett.* **2015**, 15, 6985.
- [30] P. Albella, M. A. Poyli, M. K. Schmidt, S. A. Maier, F. Moreno, J. J. Saenz, J. Aizpurua, *J. Phys. Chem. C* **2013**, 117, 13573.
- [31] R. M. Bakker, D. Permyakov, Y. F. Yu, D. Markovich, R. Paniagua-Dominguez, L. Gonzaga, A. Samusev, Y. Kivshar, B. Luk'yanchuk, A. I. Kuznetsov, *Nano Lett.* **2015**, 15, 2137.
- [32] R. Regmi, J. Berthelot, P. M. Winkler, M. Mivelle, J. Proust, F. Bedu, I. Ozerov, T. Begou, J. Lumeau, H. Rigneault, M. F. Garcia-Parajo, S. Bidault, J. Wenger, N. Bonod, *Nano Lett.* **2016**, 16, 5143.
- [33] J. Yan, P. Liu, Z. Lin, H. Wang, H. Chen, C. Wang, G. Yang, *ACS Nano* **2015**, 9, 2968.
- [34] P. Albella, T. Shibanuma, S. A. Maier, *Sci. Rep.* **2015**, 5, 18322.
- [35] J. van de Groep, T. Coenen, S. A. Mann, A. Polman, *Optica* **2016**, 3, 93.
- [36] J. van de Groep, A. Polman, *Opt. Express* **2013**, 21, 26285.
- [37] M. A. van de Haar, J. van de Groep, B. J. Brenny, A. Polman, *Opt. Express* **2016**, 24, 2047.
- [38] T. Coenen, J. van de Groep, A. Polman, *ACS Nano* **2013**, 7, 1689.
- [39] A. Mirzaei, A. E. Miroshnichenko, *Nanoscale* **2015**, 7, 5963.
- [40] M. Quinten, *Optical Properties of Nanoparticle Systems: Mie and Beyond*, Wiley, New York **2011**.
- [41] J. M. Dallesasse, N. Holonyak, A. R. Sugg, T. A. Richard, N. El-Zein, *Appl. Phys. Lett.* **1990**, 57, 2844.
- [42] S. Gehrsitz, F. K. Reinhart, C. Gourgon, N. Herres, A. Vonlanthen, H. Sigg, *J. Appl. Phys.* **2000**, 87, 7825.
- [43] T. Coenen, B. J. M. Brenny, E. J. Vesseur, A. Polman, *MRS Bull.* **2015**, 40, 359.
- [44] E. S. Barnard, T. Coenen, E. J. Vesseur, A. Polman, M. L. Brongersma, *Nano Lett.* **2011**, 11, 4265.
- [45] V. Myroshnychenko, J. Nelayah, G. Adamo, N. Geuquet, J. Rodriguez-Fernandez, I. Pastoriza-Santos, K. F. MacDonald, L. Henrard, L. M. Liz-Marzan, N. I. Zheludev, M. Kociak, F. J. Garcia de Abajo, *Nano Lett.* **2012**, 12, 4172.
- [46] F. J. Garcia de Abajo, *Rev. Mod. Phys.* **2010**, 82, 209.
- [47] A. Losquin, M. Kociak, *ACS Photonics* **2015**, 2, 1619.